Atomic order and cluster energetics of a 17 w.t.% Si-based glass versus the liquid phase

G.S.E. Antipas[1], L. Temleitner[2,3], K. Karalis[1],
L. Pusztai[2] and A. Xenidis[1]

[1]School of Mining Engineering and Metallurgy
National Technical University of Athens
Zografou Campus, Athens 15780
Greece
Tel. +30 210 7722388
Email: gantipas@metal.ntua.gr

[2]Institute for Solid State Physics and Optics,
Wigner Research Centre for Physics,
Hungarian Academy of Sciences,
H-1525 Budapest, P.O. Box 49
Hungary

[3]Japan Synchrotron Radiation Research Institute (SPring-8/JASRI)
1-1-1 Kouto, Sayo
Hyogo 679-5198, CREST-JST
Japan

Abstract
Aerodynamic levitation of a multi component 17 w.t.% Si glass formed by rapid quenching of the melt phase was studied by high resolution X-ray diffraction (XRD) and Reverse Monte Carlo (RMC) modeling. The main local atomic order features comprised of interactions between Si, Fe and Mg polyhedra, the stereochemistry of which was on a par with literature. Both the glass and the liquid state appeared to consist of the same fundamental Si-O, Fe-O and Mg-O clusters, with only the relative number of each varying between the two. Transition from liquid to the glass involved a 3-fold decrease in uncoordinated O (to within the first minimum of the total $g(r)$) and a marked increase of Fe-Si-Mg polyhedra bridging O. Octahedral Fe coordination was not suggested by the RMC data. All-electron open-shell Density Functional Theory (DFT) calculations of the most prominent clusters suggested independence between the Fe oxidation state and its polyhedra O-coordination. Of secondary thermodynamic importance were indications of network-forming Fe^{2+} and Fe^{3+} distorted trigonal and tetrahedral polyhedra. In all occasions, the Fe ferrous and ferric states involved comparable binding energies within similar clusters which indicate a dynamic equilibrium between the two.

1. Introduction

Multicomponent aluminosilicate oxides in the amorphous state are of ubiquitous engineering importance, largely as much as they are intractable in terms of their atomic structure. Applications related to these oxides are invariably dependent on their mesoscale properties, such as viscosity and thermal conductivity, which, in turn, have been correlated to the number and movement of cations through the silicate network and to the availability of free (not fully coordinated) oxygen atoms. In alkaline earth oxides, the basicity of the melt has been empirically related to the mass ratio of $(CaO+MgO)/SiO_2$ [1] and appears to be inversely proportional to viscosity [2, 3]. Certainly, complementary effects between network formers and modifiers are dependent on ionic radii, valence and electron orbitals [4]. Of particular interest, the melt oxide conductivity has been linked to the concentration of (ferric) Fe^{3+} ions while the existence of the latter appears to depend on the Fe^{3+}/Fe^{2+} redox equilibrium [5-7] the kinetics of which are greatly affected by network-modifying cations [6, 8, 9]. Perhaps counter-intuitively, Fe was reported to assume either in a network modifying or network forming role depending on its oxygen coordination rather than the oxide elemental concentration [6]. According to experimental observations, Fe tetrahedral (oxygen) coordination is achieved for all ferric iron when the $Fe^{3+}:Fe^{2+}$ ratio exceeds 1:1 [10]. Octahedral Fe^{2+} is widely assumed to act as a network modifier, whereas there is broad consensus, albeit not based on atomic studies, that tetrahedral Fe^{2+} acts as a network former [7, 9]. To address the issue of atomic structure in complex, high temperature oxide systems, we have reported on the short-range order of a composite Fe-Si-Al-Ca-Mg-Cr-Cu-Ni oxide system in the liquid phase ($1500°C$) studied via aerodynamic levitation, high-energy XRD and subsequent RMC simulations [11]. In that study, structural analysis of the RMC supercells revealed the presence a silicate polymerized network consisting of distorted SiO_4 tetrahedra chains terminated by AlO_4 units. Network modifying Fe and Mg atoms within the silicate cavities provided the necessary charge neutrality by competing for network-modifying positions [12], with the Mg species exhibiting a greater affinity to the silicate bridging oxygens than Fe. Cr, although not assuming a network forming role, maintained a 4-fold coordination, effectively reducing the amount of bridging O atoms in the melt. The most probable atomic cluster, characteristic of short-range coordination, was found to consist of Fe and Mg atoms interchangeably connecting a silicate network of a four SiO_4 tetrahedra terminated by an AlO_4 unit.

In the current study, we extend our previous work into the glassy state by discussing the short range order of the Si-Fe-Al-Ca-Mg-Cr-Cu-Ni oxide glass as rapidly solidified by aerodynamic levitation after laser melting. The discussion is in direct comparison with the liquid state (as levitated) of the same material [11]. We proceed to correlate the glass high-energy XRD to the liquid state by means of Reverse Monte Carlo [13] and we qualify this comparison with DFT calculations of the most prominent cluster formations, in which focus is on the oxidation state of Fe and the role of network modifying Mg. We conclude by generalizing on the glass silicate network while rooted in first principles.

2. Materials and methods

A detailed account of collection and processing of the slag from the industrial smelting plant of LARCO S.A., in Larymna, Greece has already been given in [11]. For the sake of completeness we reproduce here that the system is Fe-rich by approximately 24.3% with a Si content of 17.6% and secondary inclusions of Mg, Al, Ca and Cr in the range 2.3-3.9%; concentration of each atomic species in the material is summarized in Table 1,

while more detailed chemical analyses of the same system can be found in [11] and references therein.

A total of 15.5 mg of the slag sample was aerodynamically levitated by a compressed air flow initiating from a cooled conical nozzle, and was melted by a CO_2 laser with a maximum power of 100W at the BL04B2 beamline at SPring-8, Japan [14, 15]. Upon rapid cooling, the slag solidified to a final (near-spherical) diameter of 2.05 ± 0.02 mm, for which the corresponding density was estimated to 3.44 g/cm^3, in agreement with the specific gravity-inferred density of the system as measured in [11]. The sample was then wrapped in Kapton foil and was measured in diffractometer flat-plate geometry at a wavelength of 0.20194 Å (61.39 keV). Based on raw data, corrected for background, polarization, absorption and inelastic scattering, the total structure factor was then calculated, normalized by the square of the average atomic form factor; the latter calculation was performed by a custom built subroutine running on the IGOR PRO software platform. For a more detailed account of experimental settings as well as data analysis, the reader is referred to [11].

RMC simulations were performed via RMC_POT [16]. In RMC, the variance between the experimentally estimated and a calculated set of total structure factor data is minimized by a Metropolis importance sampling scheme, subject to the molar fractions and the X-ray scattering coefficients of each atomic species in the system. The atomic coordinates of the melt supercell presented in [11] were used as the starting configuration for the present simulation which was performed for a supercell of 3001, atoms in a cubic box with periodic boundary conditions imposed, keeping the number density fixed at 0.084 atoms/Å^3. The number of each atom species in the RMC simulation is listed in Table 2.

DFT calculations were performed with the Amsterdam density functional (ADF) program [17, 18] within the realm of the generalized gradient approximation (GGA). Electron exchange and correlation was addressed by the BLYP [19, 20] functional. Single-electron wavefunctions were expanded using the TZP and TZ2P uncontracted Slater-type orbital (STO) basis set, (a triple-ζ basis set with one and two sets of polarization functions respectively) for all atoms. All calculations were spin unrestricted by fixing an electron analogy of 13 α- to 10 β- and vice versa for every Fe^{3+} ion; in a similar manner, unrestricted DFT calculations were carried out for Fe^{2+} ions.

3. Results and Discussion

In the pre-levitation XRD spectrum of the material, presented originally in [11] and reproduced in Fig. 1, the main phases identified were fayalite (Fe_2SiO_4), forsterite (Mg_2SiO_4), magnetite (Fe_3O_4), christobalite/tridymite (SiO_2), chromite ($FeCr_2O_4$), ferrosilite ($Ca_{0.5}Fe_{1.5}Si_2O_6$) and magnesioferrite ($Al_{0.47}Fe_{1.52}MgO_4$), in agreement with previous XRD studies of the system [21]. The XRD spectrum, of the aerodynamically cooled sample, characteristic of the material's glass state, is shown in Fig. 2, also in comparison to the liquid (levitated) [11].

Table 3 lists details of the RMC simulation performed in this study, contrasted against that of the liquid state. Fig. 3 is a comparison of the RMC-estimated vs. the experimental total structure factor for both the glass and liquid. For the glass, XRD offered satisfactory resolution up to approximately 12 Å^{-1}; the material's S(Q) shape below 0.7 Å^{-1} is suggestive of long-range ordering, while short-range order is flagged by the fluctuations between 5.5 and 11.5 Å^{-1}.

Fig. 4 depicts the total g(r), as a Fourier transform of the experimental total structure factor, S(Q); also shown are the principal partials that make up short-range order. Corresponding first coordination shell radii (Å) for selected partials, for both the

liquid and glass phase, are listed in Table 4, while bond angle distribution peaks are presented in Table 5. From Fig. 4, short-range order is apparent up to an inter-atomic distance of 6 Å. Table 6 presents principal coordination features within the first minimum of the total RDF, for both the glass and the liquid phase. Differences arising from the transition from the melt to the glass will be discussed in the forthcoming sections; here we note that in the glass state, both network forming as well as network modifying cations are primarily tetrahedral in respect with oxygen ligands. However, the glass is essentially defined by the marked increase of tetrahedral Fe [7].

As seen in Table 4, the glass RMC Si-Si and Fe-Fe partials are somewhat underestimated compared to relevant literature and on a par with the liquid state. Si tetrahedra are near-ideal on the basis of their O-Si-O angle of 107°, while distortion is flagged from corresponding small angles for the Al, Cr (93°) as well as Mg and Fe (87°) polyhedra (see Table 5). Linkage Si-O-Si and Al-O-Al angles of 117° and 77° signify corner and edge/face tetrahedra sharing, respectively. Transition from the liquid to the glass is accompanied by an overall increase of oxygen coordination for both network formers and modifiers, as portrayed in Table 6; the most striking such feature is in regard with Fe (see Table 6), for which almost 80% is 4- or 5-fold coordinated in broad agreement with data discussed in [6, 7] and references therein. The same behaviour is observed for Mg, while for both cations there is a fraction of 3-fold coordination, possibly of distorted trigonal planar configuration. Cr and Al in the glass state both remain tetrahedral upon transition from the liquid.

The oxygen environment of the glass is presented in Table 7, in conjunction with the liquid; upon rapid solidification, there is a marked decrease of non-bridging oxygens (NBO) as well as uncoordinated oxygens; more precisely, Si NBO's have decreased from 14.6% to 9.2%, Al NBO's have decreased from 2.4% to 1.2%, while uncoordinated (to within the first minimum of the total g(r)) oxygens are reduced from 5.5% to 1.8%. At the same time, a modest increase of the Fe-Si, Fe-2Si and Si-Mg-Al cluster bridging oxygens (BO) and a marked increase of Fe-Fe, Fe-Si-Mg, Fe-Mg, Si-2Fe BO's formulate the glass long-range order. Perhaps surprisingly, the coordination number for the Fe-Fe and Fe-Mg partials remains constant and equal to 3 and 1, respectively, for both the glass and the liquid state. In contrast, Fe-Si coordination increases to 3 in the glass from a value of 2 in the liquid state. As seen in Table 7, out of the top 80% of oxygen coordination features in the glass, a mere 9% is related to Al, while the bulk is comprised of interactions between Fe, Si and Mg; the same finding stands for the liquid phase. We, thus, concentrate our attention to Fe, Si and Mg clusters and we proceed to discuss these in the context of DFT. A number of Si, Fe and Mg oxide clusters were relaxed in the gas phase and are listed in Table 8 along with their respective binding energies normalized by number of electrons in every cluster. The clusters were chosen on the basis of the most frequent linkages as flagged by the oxygen environment shown in Table 7; consequently, they involved coordination combinations of 3 and 4 for Si-O, 3, 4 and 5 for Fe-O and 2, 3, and 4 for Mg-O. Simulations were run for both the ferrous and ferric state in every conformer. Based on cluster energetics, the average oxidation state of Fe was calculated in two manners; in the first, the oxidation state was expressed as the ratio $(2 \cdot E_b^{2+} + 3 \cdot E_b^{3+})/\Sigma E_b$, where E_b^{2+} and E_b^{3+} are the binding energy sums over all clusters that favour the ferrous and ferric state, respectively, and ΣE_b is the sum of all binding energies for simulations 1 to 41, the latter concerning clusters all of which share the same corner (oxygen atom). In this manner the average oxidation state was estimated as 2.28. Similarly, the average oxidation state of Fe for clusters in which the Fe polyhedron is surrounded by Si and Mg clusters, again bound by single corner-sharing (simulations 42 to 47) was found to be 2.31. In the second manner, the binding energy ratios for

simulations 1 to 41 were weighted by the fraction of each coordination feature as presented in Table 7. In this manner, the (weighted) average oxidation state of Fe was found to be 2.32 in both the glass and the liquid phase.

Figure 5 illustrates the effect of DFT-calculated Fe coordination by oxygen (inclusive of second neighbours) in respect to the binding energy for the range of clusters listed in Table 8. As deduced from the data, the most thermodynamically favoured clusters involve the ferrous Fe state; in fact all such clusters terminate silicate chains and, by extension, the Fe ions can be characterized as charge-balancing network modifiers. As seen in Figure 5, the easiest formed among clusters (with an associated binding energy of $-2.099 \cdot 10^{-2}$ a.u.) is a ferrous Fe centered tetrahedron in single corner linkage to three- and four-fold coordinated Si polyhedra. In contrast, network-forming Fe clusters surrounded by Si polyhedra, still preferentially engage the ferrous Fe state but are now less thermodynamically favoured, as seen in the cluster indexed 42 (see Figure 5) with an associated binding energy of $-1.822 \cdot 10^{-2}$ a.u.. In actuality, for every conformer in Table 8, the ferrous and ferric Fe states may indeed co-exist, while thermodynamic preference is always on the ferrous state [6]. This trend is very much consistent across a range of Fe coordination by oxygen of between 3 and 5 and Fe coordination by Si of 1 to 3. Notably, substitution of Si by Mg clusters has no noticeable effect either on the mean oxidation state of Fe or on the thermodynamic preference of the system towards the ferrous state; this leads us to conclude that Fe^{2+} naturally tends to assume a network modifying role regardless of its oxygen coordination, while it is in direct charge-balancing competition with neighbouring Mg polyhedra [8], a trend the origins of which we have already touched upon in [11]. Formation of Fe diclusters is also possible, albeit with reduced thermodynamic probability and at a Fe average oxidation state of 2.53, as calculated based on binding energetics; hence Fe diclusters favour equilibrium of the ferrous and ferric state under the oxygen coordination studied [6].

Studies of Fe polyhedra-centered clusters (DFT simulations 42 to 47 in Table 8) reveal a trend, overall similar to that in Fe polyhedra-terminated clusters; the ferrous state is again thermodynamically favoured, even in tetrahedral coordination, although in close co-existence with the ferric state. Both Fe states exhibit their highest affinity as network formers coordinated by three Si tetrahedra (DFT simulations 42 and 45 in Table 8). The gradual introduction of Mg polyhedra in corner-sharing linkage to trigonal off-planar Fe conformers appears to have some stabilizing effect of the ferric Fe state [8]; however more DFT work needs to be carried out in order to generalize this observation into a trend.

4. Conclusions

A multi component silicate glass formed by rapid quenching of the melt phase during aerodynamic levitation was studied by high resolution XRD and RMC modeling. Local atomic order features of the glass were on a par with literature and both states appeared to consist of the same fundamental clusters, with the relative number of each varying between the glass and the melt. Transition from liquid to glass involved a 3-fold decrease in uncoordinated O (to within the first minimum of the total g(r)) and a marked increase of Fe-Si-Mg polyhedra bridging O. Spin unrestricted DFT calculations for Si-Fe-Mg oxide clusters suggested that the oxidation state of Fe does not depend on its polyhedra coordination, while Fe^{2+} was found to assume primarily network modifying positions in competition with Mg. In all occasions, the Fe ferrous and ferric states revealed comparable binding energies within similar clusters which indicate a dynamic thermodynamic equilibrium.

5. Acknowledgements

6. References

[1] Y.M. Kuo, C.T. Wang, C.H. Tsai, L.C. Wang, Chemical and physical properties of plasma slags containing various amorphous volume fractions, Journal of hazardous materials, 162 (2009) 469-475.

[2] A. Kondratiev, E. Jak, Modeling of viscosities of the partly crystallized slags in the Al2O3-CaO-'FeO'-SiO2 system, Metallurgical and Materials Transactions B: Process Metallurgy and Materials Processing Science, 32 (2001) 1027-1032.

[3] Y.S. Lee, J.R. Kim, S.H. Yi, D.J. Min, Viscous behaviour of CaO-SiO2-Al2O3-MgO-FeO slag, VII International Conference on Molten Slags Fluxes and Salts, (2004).

[4] P. Hudon, D.R. Baker, The nature of phase separation in binary oxide melts and glasses. I. Silicate systems, Journal of Non-Crystalline Solids, 303 (2002) 299-345.

[5] D. Virgo, B.O. Mysen, The structural state of iron in oxidized vs. reduced glasses at 1 atm: A57Fe Mössbauer study, Physics and Chemistry of Minerals, 12 (1985) 65-76.

[6] B.O. Mysen, The structural behavior of ferric and ferrous iron in aluminosilicate glass near meta-aluminosilicate joins, Geochimica et Cosmochimica Acta, 70 (2006) 2337-2353.

[7] G. Giuli, R. Alonso-Mori, M.R. Cicconi, E. Paris, P. Glatzel, S.G. Eeckhout, B. Scaillet, Effect of alkalis on the Fe oxidation state and local environment in peralkaline rhyolitic glasses, American Mineralogist, 97 (2012) 468-475.

[8] A. Wiedenroth, C. Rüssel, The effect of MgO on the diffusivity of iron and the incorporation of iron in soda-magnesia-aluminosilicate melts, Journal of Non-Crystalline Solids, 347 (2004) 180-186.

[9] K.E. Kelsey, J.F. Stebbins, D.M. Singer, G.E. Brown, J.L. Mosenfelder, P.D. Asimow, Cation field strength effects on high pressure aluminosilicate glass structure: Multinuclear NMR and La XAFS results, Geochimica et Cosmochimica Acta, 73 (2009) 3914-3933.

[10] G.B. Cook, R.F. Cooper, T. Wu, Chemical diffusion and crystalline nucleation during oxidation of ferrous iron-bearing magnesium aluminosilicate glass, Journal of Non-Crystalline Solids, 120 (1990) 207-222.

[11] G.S.E. Antipas, L. Temleitner, K. Karalis, S. Kohara, L. Pusztai, A. Xenidis, A containerless study of short-range order in high-temperature Fe–Si–Al–Ca–Mg–Cr–Cu–Ni oxide systems, Journal of Molecular Structure, 1019 (2012) 151-158.

[12] Y.Q. Wu, S.P. Huang, J.L. You, G.C. Jiang, Molecular dynamics of structural properties of molten CaO-SiO2 with varying composition, Trans. Non-Ferrous Met. Soc. China, 12 (2002).

[13] O. Gereben, L. Pusztai, RMC_POT: A computer code for reverse monte carlo modeling the structure of disordered systems containing molecules of arbitrary complexity, Journal of Computational Chemistry, 33 (2012) 2285-2291.

[14] M. Isshiki, Y. Ohishi, S. Goto, K. Takeshita, T. Ishikawa, High-energy X-ray diffraction beamline: BL04B2 at SPring-8, Nuclear Instruments and Methods in Physics

Research Section A: Accelerators, Spectrometers, Detectors and Associated Equipment, 467-468 (2001) 663-666.

[15] S. Kohara, K. Suzuya, High-energy X-ray diffraction studies of disordered materials, Nuclear Instruments and Methods in Physics Research, Section B: Beam Interactions with Materials and Atoms, 199 (2003) 23-28.

[16] P. Gereben O., L., RMC_POT, a computer code for Reverse Monte Carlo modeling the structure of disordered systems containing molecules of arbitrary complexity, Journal of Computational Chemistry, (2012).

[17] SCM, Amsterdam Density Functional program, Theoretical Chemistry, Vrije Universiteit, Amsterdam, http://www.scm.com., in.

[18] E.J. Baerends, D.E. Ellis, P. Ros, Self-consistent molecular Hartree-Fock-Slater calculations I. The computational procedure, Chemical Physics, 2 (1973) 41-51.

[19] A.D. Becke, Density-functional exchange-energy approximation with correct asymptotic behavior, Physical Review A, 38 (1988) 3098-3100.

[20] C. Lee, W. Yang, R.G. Parr, Development of the Colle-Salvetti correlation-energy formula into a functional of the electron density, Physical Review B, 37 (1988) 785-789.

[21] K. Komnitsas, D. Zaharaki, V. Perdikatsis, Geopolymerisation of low calcium ferronickel slags, Journal of Materials Science, 42 (2007) 3073-3082.

[22] P. Ganster, M. Benoit, J.M. Delaye, W. Kob, Structural and vibrational properties of a calcium aluminosilicate glass: Classical force-fields vs. first-principles, Molecular Simulation, 33 (2007) 1093-1103.

[23] P. Ganster, M. Benoit, W. Kob, J.M. Delaye, Structural properties of a calcium aluminosilicate glass from molecular-dynamics simulations: A finite size effects study, Journal of Chemical Physics, 120 (2004) 10172-10181.

[24] C. Huang, A.N. Cormack, The structure of sodium silicate glass, The Journal of Chemical Physics, 93 (1990) 8180.

[25] T. Kondratowicz, Structural changes in sodium-calcium-silicate glass after adding Si 3N4, Optica Applicata, 37 (2007) 41-50.

[26] M. Taylor, G.E. Brown Jr, Structure of mineral glasses-I. The feldspar glasses NaAlSi 3O 8, KAlSi 3O 8, CaAl 2Si 2O 8, Geochimica et Cosmochimica Acta, 43 (1979) 61-75.

[27] M. Taylor, G.E. Brown Jr, Structure of mineral glasses-II. The SiO 2NaAlSiO 4 join, Geochimica et Cosmochimica Acta, 43 (1979) 1467-1473.

[28] X. Yuan, A.N. Cormack, Si-O-Si bond angle and torsion angle distribution in vitreous silica and sodium silicate glasses, Journal of Non-Crystalline Solids, 319 (2003) 31-43.

[29] E.T. Kang, S.J. Lee, A.C. Hannon, Molecular dynamics simulations of calcium aluminate glasses, Journal of Non-Crystalline Solids, 352 (2006) 725-736.

[30] W. Li, S.H. Garofalini, Molecular dynamics simulation of lithium diffusion in Li 2O-Al2O3-SiO2 glasses, Solid State Ionics, 166 (2004) 365-373.

[31] M. Liška, J. Macháče, P. Perichta, O. Gedeon, J. Pilát, Thermochemical modelling and Ab initio molecular dynamics simulations of calcium aluminate glasses, Ceramics - Silikaty, 52 (2008) 61-65.

[32] A. Nukui, U. Shimizugawa, S. Inoue, H. Ozawa, R. Uno, K. Oosumi, A. Makishima, A structural study of Y2O3Al2O3SiO2 glass employing partial RDFs obtained by anomalous scattering, Journal of Non-Crystalline Solids, 150 (1992) 376-379.

[33] P. Perichta, M. Liška, J. Macháček, O. Gedeon, MD structural study of 23Y2O3-77Al2O 3 and 23La2O3-77Al2O3 glasses, Ceramics - Silikaty, 53 (2009) 52-54.

[34] S.M. Haile, B.J. Wuensch, X-ray diffraction study of K3NdSi7O17: A new framework silicate with a linear Si-O-Si bond, Acta Crystallographica Section B: Structural Science, 56 (2000) 773-779.

[35] J. Jin, S. Sakida, T. Yoko, M. Nogami, The local structure of Sm-doped aluminosilicate glasses prepared by sol-gel method, Journal of Non-Crystalline Solids, 262 (2000) 183-190.

[36] T. Fujiwara, H.S. Chen, Y. Waseda, On the structure of Fe-B metallic glasses of hypereutectic concentration, Journal of Physics F: Metal Physics, 11 (1981) 1327-1333.

[37] P.K. Hung, N.V. Hong, L.T. Vinh, Diffusion and structure in silica liquid: A molecular dynamics simulation, Journal of Physics Condensed Matter, 19 (2007).

[38] G. Gutiérrez, A.B. Belonoshko, R. Ahuja, B. Johansson, Structural properties of liquid Al2O3: A molecular dynamics study, Physical Review E - Statistical Physics, Plasmas, Fluids, and Related Interdisciplinary Topics, 61 (2000) 2723-2729.

Table captions

Table 1. Concentration (% w.t.) of each atomic species.

Table 2. Number of atoms for each species in the RMC simulations.

Table 3. RMC run details for the glass phase [11], designated as RMC_G. For comparison purposes, the same details for the RMC run of the liquid phase, designated as RMC_L, are also presented. Coordination constraints were not set for either run. RMC fit refers to the overall least squares fit achieved between the calculated and the experimental total structure factor.

Table 4. First coordination shell radius (Å) for selected partials for both the liquid and glass phase. A comparison with literature data is also shown.

Table 5. Peak position of the bond angle distribution (degrees) for selected liquid and glass partials. A comparison with literature data is also shown.

Table 6. Principal coordination features within the first minimum of the total RDF. The feature is one of coordination of the first atom shown (central atom) with atoms of the second atom. CN is total coordination number. Percentage of each feature is relative to the total number of coordination features observed for the central atom.

Table 7. RMC-generated oxygen atom environment for the glass in comparison with the liquid state. Each coordination feature is represented as a percentage of all features for the oxygen species.

Table 8. DFT-calculated binding energies for corner-sharing polyhedra in respect to the oxidation state of Fe. The field 'Index' refers to the DFT simulation run.

Figure captions

Figure 1. Pre-levitation XRD spectrum.

Figure 2. XRD spectra of the liquid [11] and glass phase.

Figure 3. Experimental (lines) and RMC-generated (points) total structure factors of the liquid [11] and glass phase.

Figure 4. Total g(r) of the glass and liquid [11] phase, as a Fourier transform of the corresponding total structure factors.

Figure 5. DFT-calculated Fe coordination by oxygen atoms inclusive of second neighbours (grey triangles), in respect to the binding energy for the range of clusters listed in Table 8. The energies shown are total binding energies normalized by the number of electrons in every cluster. A 5th order polynomial (black solid line) has been fitted to the points in order to highlight the trend. Each cluster shown involves a ferrous Fe ion and represents the ground state configuration in its group; the cluster energies are also shown in the figure along with their index, corresponding to Table 8. The double arrow highlights the energy range within which the Fe ferric state increasingly participates in thermodynamically favourable clusters; however, all conformers of interest, i.e. below $1.8 \cdot 10^{-2}$ a.u., including the ones shown, are based on the Fe^{2+} ion. Atom colour notation is as follows: orange – Fe, bronze – Si, grey - Mg and red – O.

Table 1. Concentration (% w.t.) of each atomic species.

Fe	Si	Al	Mg	Ca	Cr
24.379	17.611	3.108	3.925	2.386	2.445

Table 2. Number of atoms for each species in the RMC simulations.

Fe	Si	Al	Mg	Ca	Cr	O
308	445	98	131	42	32	1945

Table 3. RMC run details for the glass phase, designated as RMC_G. For comparison purposes, the same details for the RMC run of the liquid phase [11], designated as RMC_L, are also presented. Coordination constraints were not set for either run. RMC fit refers to the overall least squares fit achieved between the calculated and the experimental total structure factor. 100 – Rwp denotes the overall RMC fit where Rwp is the weighted-profile R value.

Designation	Number of Atoms	Coordination constraint	Box length (Å)	Number density (atoms/Å^3)	Density (g/cm^3)	100-Rwp (%)
RMC_G	3001	None	32.94266	0.084	3.26	93.3
RMC_L	3001	None	34.07278	0.076	2.94	95.1

Table 4. First coordination shell radius (Å) for selected partials for both the liquid and glass phase. A comparison with literature data is also shown.

Partial	Glass	Glass literature	Liquid [11]	Liquid literature [11]
Si-O	1.71	1.6 [22-28]	1.72	1.6-1.65
Al-O	1.85	1.69-1.82 [22, 25, 27, 29-33]	1.86	1.72-2.9
Cr-O	1.85	-	1.86	-
Mg-O	1.92	2 [11]	1.93	1.81-2
Fe-O	1.99	-	2.00	2
Ca-O	2.35	2.3-3.1 [25, 29, 32]	2.35	2.31-2.5
Fe-Si	2.35	-	2.35	-
O-O	2.70	2.59-2.85 [24-26, 29-31, 33]	2.77	2.35-3.2
Si-Si	2.84	3.08-3.2 [23, 24, 26, 27, 29, 34, 35]	2.56	2.5-3.165
Fe-Fe	3.26	4.1-4.4 [36]	3.12	-

Table 5. Peak position of the bond angle distribution (degrees) for selected liquid and glass partials. A comparison with literature data is also shown.

Partial	Glass	Glass literature	Liquid [11]	Liquid literature
O-Si-O	107	109 [24]	108	105 [37]
O-Al-O	93	107.6-109.5 [22, 23, 29]	95	95 [38]
O-Cr-O	93	-	95	-
O-Mg-O	87	-	88	-
O-Fe-O	87	-	87	-
Si-O-Si	117	120-180 [24]	118	144 [37]
Al-O-Al	77	-	81	115 [38]

Table 6. Principal coordination features within the first minimum of the total RDF. The feature is one of coordination of the first atom shown (central atom) with atoms of the second atom. CN is total coordination number. Percentage of each feature is relative to the total number of coordination features observed for the central atom.

Feature	Glass		Liquid	
	CN	% of feature	CN	% of feature
Si-O	3	8.30	3	8.70
	4	91.60	4	91.20
Al-O	3	6.10	3	11.20
	4	92.80	4	88.70
Fe-O			1	2.90
			2	19.10
	3	18.50	3	46.10
	4	65.50	4	30.10
	5	14.20		
Mg-O			2	15.20
	3	21.30	3	54.90
	4	65.60	4	29.00
	5	12.20		
Cr-O	4	100.00	4	100.00

Table 7. RMC-generated oxygen atom environment for the glass in comparison with the liquid state [11]. Each coordination feature is represented as a percentage of all features for the oxygen species.

Coordination feature	Glass	Liquid
1 Fe, 1 Si	15.7	13.8
1 Si	9.2	14.6
2 Si	9.0	9.8
1 Fe	6.8	7.0
1 Fe, 2 Si	5.0	3.9
1 Si, 1 Mg	4.7	4.9
2 Fe	4.7	2.9
1 Si, 1 Al	4.5	4.6
1 Fe, 1 Si, 1 Mg	3.8	2.3
1 Fe, 1 Mg	3.4	2.2
1 Mg	2.7	2.6
1 Si, 2 Fe	2.6	1.8
1 Si, 1 Fe, 1 Al	2.5	1.7
1 Fe, 1 Al	2.3	2.1
---	1.8	5.5
2 Si, 1 Mg	1.6	1.7
2 Si, 1 Al	1.5	1.6
1 Al	1.2	2.4
1 Si, 1 Mg, 1 Al	1.2	0.8

Table 8. DFT-calculated binding energies per number of electrons for corner-sharing polyhedra in respect to the oxidation state of Fe. The field 'Index' refers to the DFT simulation run.

| Index | Cluster | Binding energy (10^{-2} a.u.) | | Index | Cluster | Binding energy (10^{-2} a.u.) | |
		Fe^{2+}	Fe^{3+}			Fe^{2+}	Fe^{3+}
1	SiO_3, FeO_3	-1.833	-1.939	25	SiO_3, MgO_3, FeO_3	-1.851	-1.782
2	SiO_3, FeO_4	-1.954	-1.980	26	SiO_3, MgO_3, FeO_4	-1.867	-1.579
3	SiO_3, FeO_5	-1.908	-1.890	27	SiO_3, MgO_3, FeO_5	-1.849	-1.495
4	SiO_4, FeO_3	-1.952	-1.940	28	SiO_4, MgO_3, FeO_3	-1.881	-1.887
5	SiO_4, FeO_4	-2.003	-1.964	29	SiO_4, MgO_3, FeO_4	-1.892	-1.873
6	SiO_4, FeO_5	-1.873	-1.934	30	SiO_4, MgO_3, FeO_5	-1.918	-1.638
7	$2[SiO_3]$, FeO_3	-2.066	-2.058	31	SiO_3, MgO_4, FeO_3	-1.800	-1.754
8	$2[SiO_3]$, FeO_4	-2.068	-2.052	32	SiO_3, MgO_4, FeO_4	-1.972	-1.716
9	$2[SiO_3]$, FeO_5	-2.053	-1.866	33	SiO_3, MgO_4, FeO_5	-1.803	-1.818
10	SiO_4, SiO_3, FeO_3	-2.070	-2.055	34	SiO_4, MgO_4, FeO_3	-1.937	-1.904
11	SiO_4, SiO_3, FeO_4	-2.099	-2.072	35	SiO_4, MgO_4, FeO_4	-1.903	-1.857
12	SiO_4, SiO_3, FeO_5	-2.053	-1.688	36	SiO_4, MgO_4, FeO_5	-1.890	-1.883
13	$2[SiO_4]$, FeO_3	-2.061	-2.056	37	SiO_3, MgO_5, FeO_3	-1.920	-1.696
14	$2[SiO_4]$, FeO_4	-2.071	-1.711	38	SiO_3, MgO_5, FeO_4	-1.901	-1.833
15	$Fe^{2+}O_3$, FeO_3	-1.735	-1.720	39	SiO_3, MgO_5, FeO_5	-1.858	-1.840
16	$Fe^{2+}O_3$, FeO_4	-1.758	-1.759	40	SiO_4, MgO_5, FeO_3	-1.876	-1.656
17	$Fe^{2+}O_3$, FeO_5	-1.777	-1.780	41	SiO_4, MgO_5, FeO_4	-1.929	-1.796
18	$Fe^{3+}O_3$, FeO_3	-1.720	-1.735	42	FeO_3, $3[SiO_4]$	-1.822	-1.806
19	$Fe^{3+}O_3$, FeO_4	-1.578	-1.758	43	FeO_3, $2[SiO_4]$, MgO_3	-1.665	-1.679
20	$Fe^{3+}O_3$, FeO_5	-1.550	-1.772	44	FeO_3, SiO_4, $2[MgO_3]$	-1.298	-1.370
21	$Fe^{2+}O_4$, FeO_4	-1.800	-1.797	45	FeO_4, $3[SiO_4]$	-1.813	-1.732
22	$Fe^{3+}O_4$, FeO_5	-1.785	-1.803	46	FeO_4, $3[SiO_4]$, MgO_4	-1.695	-1.633
23	$Fe^{2+}O_5$, FeO_5	-1.683	-1.414	47	FeO_4, $2[SiO_4]$, $2MgO_4$	-1.507	-1.474
24	$Fe^{3+}O_5$, FeO_5	-1.414	-1.678				
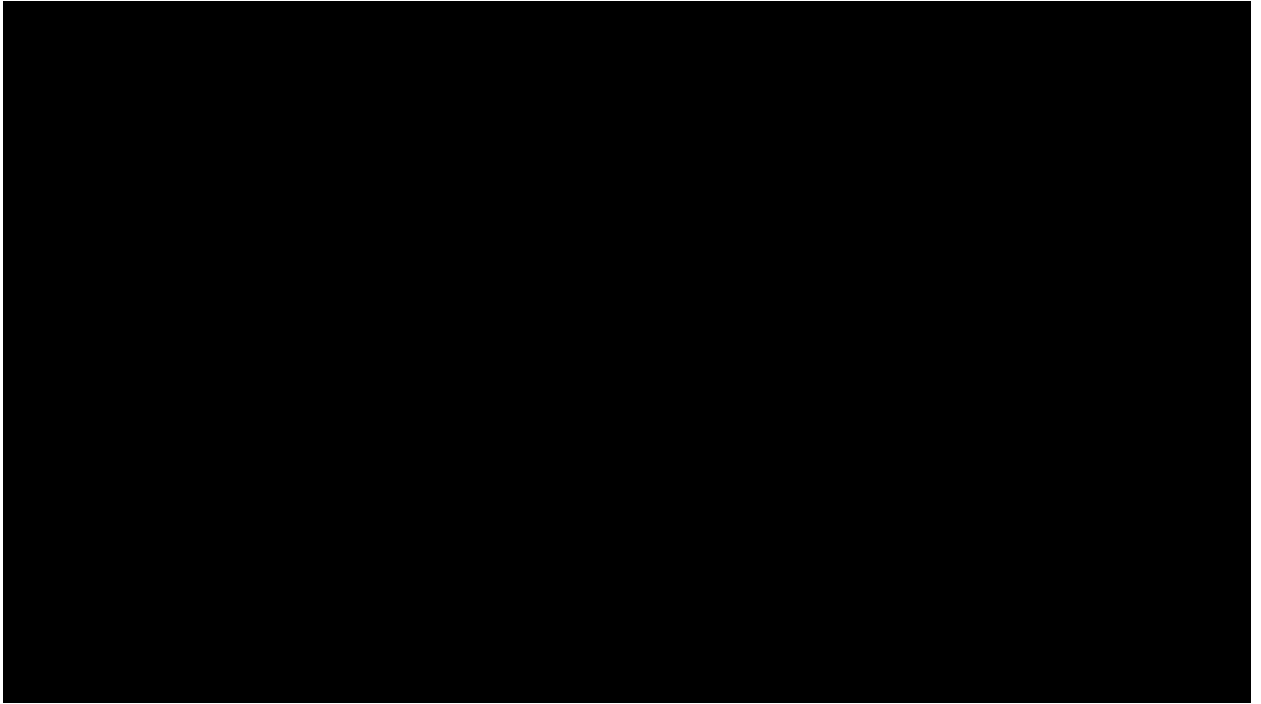
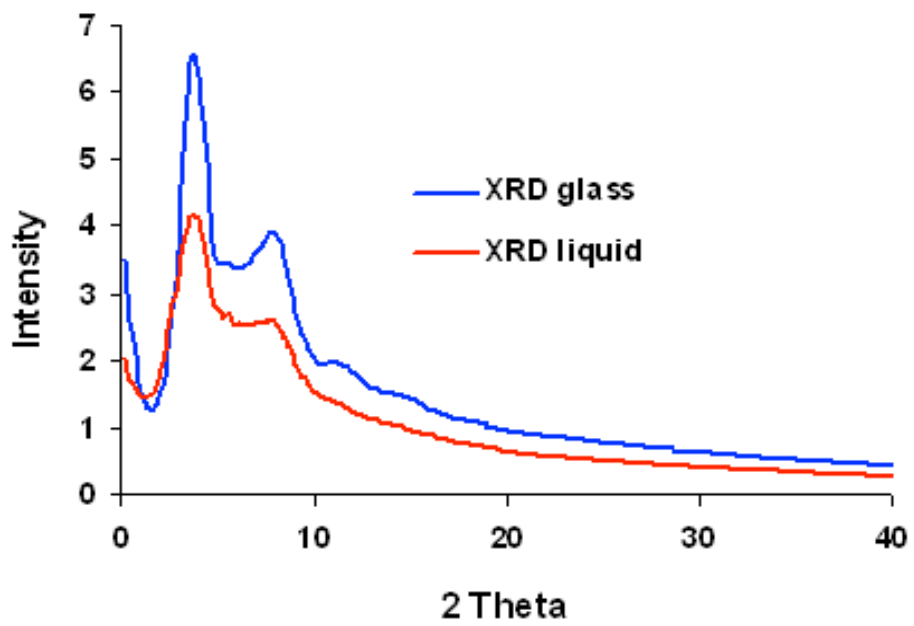Figure 1. Pre-levitation XRD spectrum.

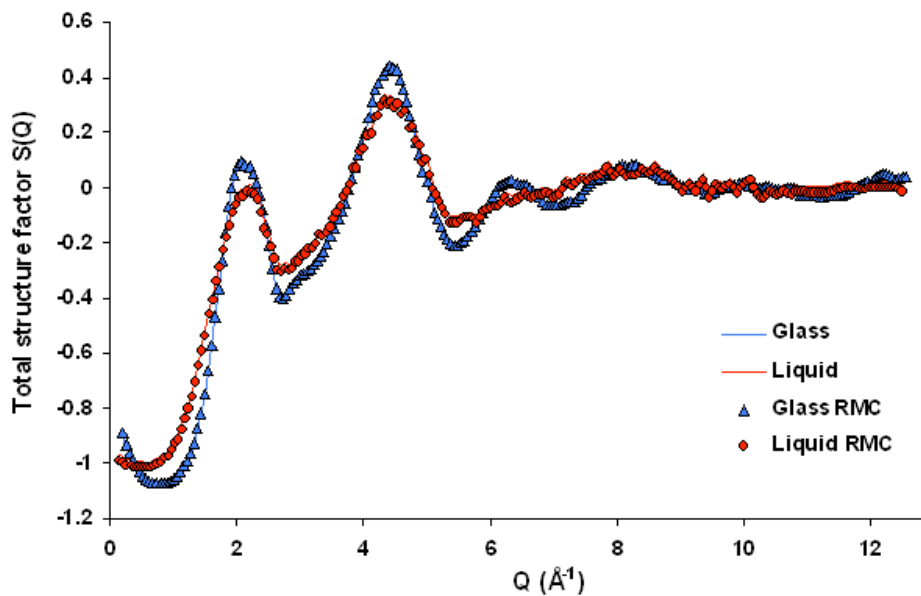Figure 2. XRD spectra of the liquid [11] and glass phase.

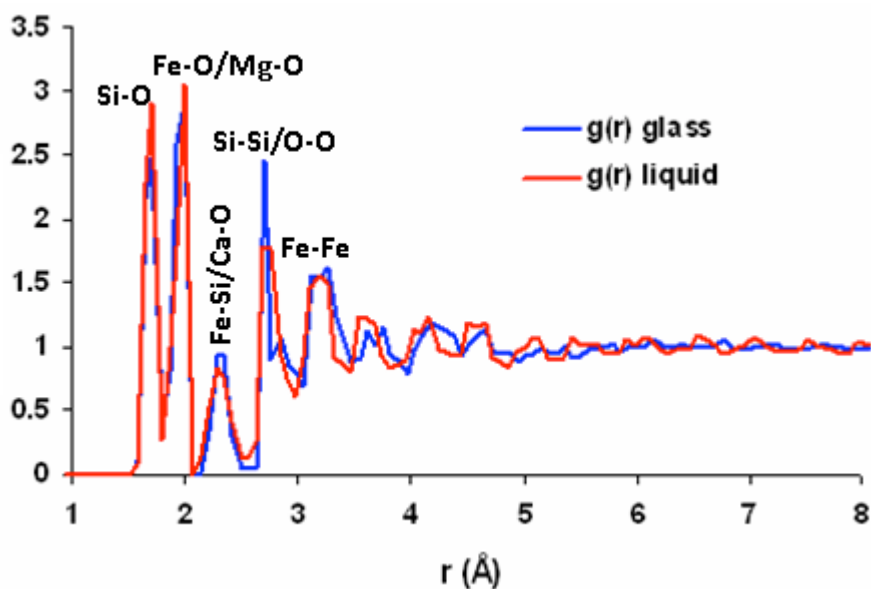Figure 3. Experimental (lines) and RMC-generated (points) total structure factors of the glass and liquid [11] phase.

Figure 4. Total g(r) of the glass and liquid [11] phase, as a Fourier transform of the corresponding total structure factors.
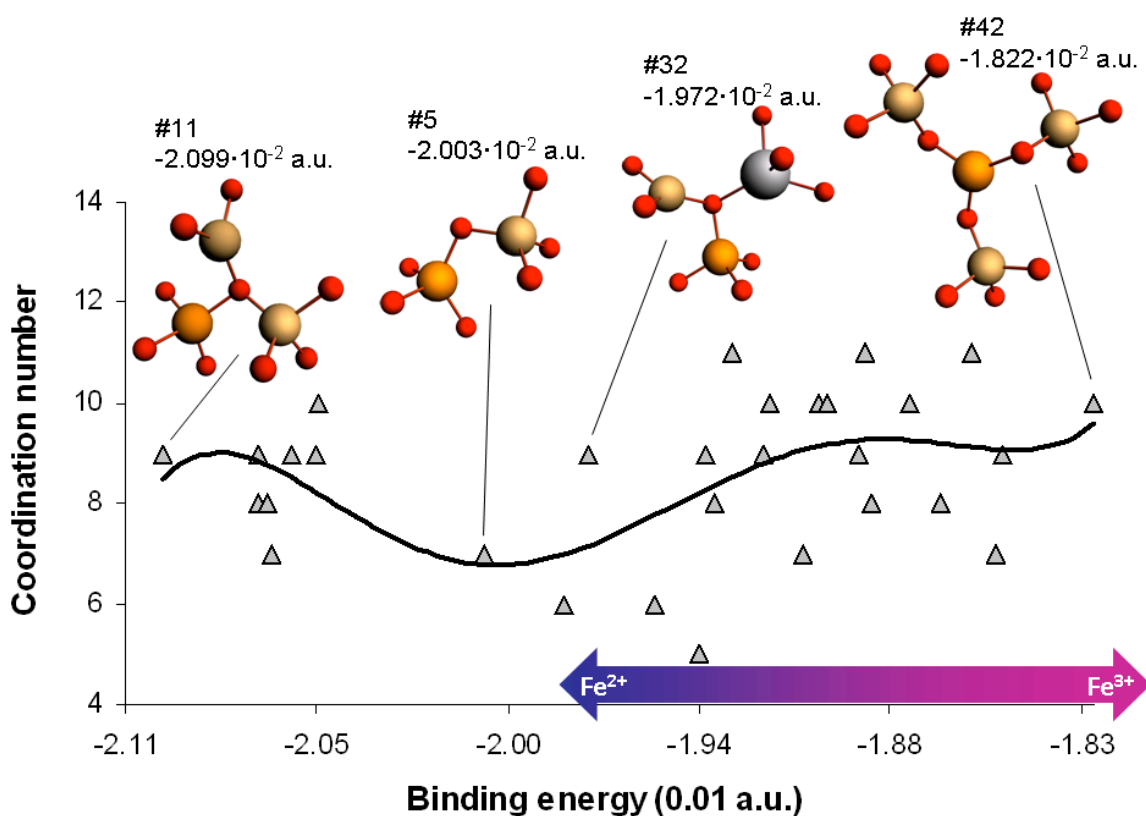
Figure 5. DFT-calculated Fe coordination by oxygen atoms inclusive of second neighbours (grey triangles), in respect to the binding energy for the range of clusters listed in Table 8. The energies shown are total binding energies normalized by the number of electrons in every cluster. A 5th order polynomial (black solid line) has been fitted to the points in order to highlight the trend. Each cluster shown involves a ferrous Fe ion and represents the ground state configuration in its group; the cluster energies are also shown in the figure along with their index, corresponding to Table 8. The double arrow highlights the energy range within which the Fe ferric state increasingly participates in thermodynamically favourable clusters; however, all conformers of interest, i.e. below $1.8 \cdot 10^{-2}$ a.u., including the ones shown, are based on the Fe^{2+} ion. Atom colour notation is as follows: orange – Fe, bronze – Si, grey - Mg and red – O.